

# Suppression of near-field coupling in plasmonic antennas on epsilon-near-zero substrates: supplementary material

CLAYTON T. DEVAULT<sup>1,4,\*,\*\*</sup>, VLADIMIR A. ZENIN<sup>2,\*</sup>, ANDERS PORS<sup>2</sup>,  
KRISHNAKALI CHAUDHURI<sup>3,4</sup>, JONGBUM KIM<sup>3,4</sup>, ALEXANDRA BOLTASSEVA<sup>3,4</sup>,  
VLADIMIR M. SHALAEV<sup>3,4</sup>, AND SERGEY I. BOZHEVOLNYI<sup>2</sup>

<sup>1</sup>Department of Physics and Astronomy, Purdue University, West Lafayette, IN 47907, USA

<sup>2</sup>SDU Nano Optics, University of Southern Denmark, Campusvej 55, DK-5230 Odense M, Denmark

<sup>3</sup>School of Electrical and Computer Engineering, Purdue University, West Lafayette, IN 47907, USA

<sup>4</sup>Birck Nanotechnology Center, Purdue University, West Lafayette, IN 47907, USA

\* Indicates equal contribution from authors

\*\* Corresponding author: cdevault@purdue.edu

Published 4 December 2018

This document provides supplementary information to “Suppression of near-field coupling in plasmonic antennas on epsilon-near-zero substrates,” <https://doi.org/10.1364/OPTICA.5.001557>. Included are the details of our Fabry-Pérot model, sample fabrication procedures, ellipsometry fitting, and numerical and experimental procedures. Furthermore, we provide additional near-field maps of antennas on Al:ZnO, and cross-section calculations of dimer antennas situated in non-dispersive materials.

## 1. FABRY-PÉROT MODEL OF A SINGLE NANOROD

The details of our semi-analytic model are discussed. We begin by considering the modes of a nanorod subject to a plane wave excitation polarized along the length of the nanorod (along  $x$ -axis, see Fig 1(a) of the main text). The origin is set to the center of the nanorod. The incident field will predominantly scatter from each end of the nanorod and will generate counter-propagating plasmonic modes  $\mathbf{u}^+$  and  $\mathbf{u}^-$ . Because of the fixed cross-section of our nanorods, we can safely assume the propagation of plasmonic modes along  $x$ -axis as  $\pm \exp(\pm ik[x \pm L/2])$ . Here,  $L$  is the length of the nanorod,  $k = 2\pi N/\lambda_0 + i/2L_{\text{prop}}$  is the propagation constant of the plasmonic mode,  $L_{\text{prop}}$  is a propagation length, and the  $\pm$  factor is associated with plasmonic modes propagation along (+) or opposite (-) to the  $x$ -axis. If the transverse field distribution of one plasmonic mode  $\mathbf{u}^+$  is described as  $[E_x(y, z), E_y(y, z), E_z(y, z)]^\dagger$ , then the counter-propagating mode  $\mathbf{u}^-$  should have electric field components  $[-E_x(-y, z), -E_y(-y, z), E_z(-y, z)]^\dagger$  since the right-hand system  $\{E_x, E_y, E_z\}$  rotates together with the propagation wave-vector. Due to the symmetry of the plasmonic mode  $E_x(-y, z) = E_x(y, z)$ ,  $E_y(-y, z) = -E_y(y, z)$ , and  $E_z(-y, z) = E_z(y, z)$ , therefore the transverse distribution of the  $\mathbf{u}^-$  mode is

$$[-E_x(y, z), E_y(y, z), E_z(y, z)]^\dagger.$$

Each plasmonic mode will traverse the length of the nanorod, reflect from the opposite end, and begin to propagate in the opposite direction; this process then continues *ad infinitum*. If we let the  $\beta = \exp(ikL)$  denote the accumulated evolution after traversing a single length of the nanorod, and let  $r$  be the complex reflection coefficient from each end of the nanorod, then the mode  $\mathbf{u}^+$  excited at one end will evolve as:

$$A^+ \sum_{j=0}^{\infty} (r\beta)^{2j} [\mathbf{u}^+ + (r\beta)\mathbf{u}^-] = A^+ \frac{[\mathbf{u}^+ + (r\beta)\mathbf{u}^-]}{1 + (r\beta)^2} \quad (\text{S1})$$

where  $A^+$  is the excitation coefficient of mode  $\mathbf{u}^+$  by the incident plane wave. Similarly, the mode  $\mathbf{u}^-$  excited at the other end with a coefficient  $A^-$  will evolve as:

$$A^- \sum_{j=0}^{\infty} (r\beta)^{2j} [\mathbf{u}^- + (r\beta)\mathbf{u}^+] = A^- \frac{[\mathbf{u}^- + (r\beta)\mathbf{u}^+]}{1 + (r\beta)^2} \quad (\text{S2})$$

The total field  $\mathbf{E}(\mathbf{x})$  is then simply a sum of Eqs. (S1) and (S2):

$$\mathbf{E}(\mathbf{x}) = \left[ \frac{A^+ + (r\beta)A^-}{1 + (r\beta)^2} \right] \mathbf{u}^+ + \left[ \frac{A^- + (r\beta)A^+}{1 + (r\beta)^2} \right] \mathbf{u}^- \quad (\text{S3})$$

Due to the symmetry of the incident field's polarization  $A^- = -A^+ = -A$ , meaning the excitation on one end is out-of-phase relatively to the excitation on the other end (however, it results in the same sign of the  $E_x$  component of each mode at both ends, since this is the polarization of the driving field). Thus, the total electric field distribution for a nanorod upon normal illumination is

$$\begin{aligned} \mathbf{E}(\mathbf{x}) &= A \frac{1 - (r\beta)}{1 + (r\beta)^2} [\mathbf{u}^+ - \mathbf{u}^-] = \frac{A}{1 + r\beta} [\mathbf{u}^+ - \mathbf{u}^-] \\ &= \frac{A}{1 + r\beta} \left[ \begin{pmatrix} E_x(y, z) \\ E_y(y, z) \\ E_z(y, z) \end{pmatrix} e^{ik(x + \frac{L}{2})} - \begin{pmatrix} -E_x(y, z) \\ E_y(y, z) \\ E_z(y, z) \end{pmatrix} e^{-ik(x - \frac{L}{2})} \right] \\ &= \frac{2A\sqrt{\beta}}{1 + r\beta} \begin{pmatrix} E_x(y, z) \cos(kx) \\ iE_y(y, z) \sin(kx) \\ iE_z(y, z) \sin(kx) \end{pmatrix} \end{aligned} \quad (\text{S4})$$

The beauty of the above semi-analytical Fabry-Pérot model is that it allows finding full three-dimensional (3D) near-field distribution without doing complicated 3D simulations, but instead it uses simple 2D simulations (modal analysis) and relatively simple 3D simulation of mode reflection (the last takes much less computational time compared to the full 3D simulation of nanorod excitation, since the simulation domain is smaller, and the effect is non-resonant, as can be seen in Fig. 1(e) in the main text). Using a single value  $A$  for normalization, we managed to accurately predict with our FP model distributions of  $E_y(x, y)$  and  $E_z(x, y)$  at any altitude  $z$  and for any antenna length (see Figure 2 in the main text). This model also predicts the position of resonances, since there the near-field will be at maximum. It is obvious that only denominator in Eq. (S4) is responsible for the resonance behavior. Neglecting weak amplitude variation of  $r$  and  $\beta$ , we find the resonance condition as  $\arg\{r\beta\} = \pi(1 + m)$ ;  $m = 0, 2, 4, \dots$ . This simplifies to Eq. (1) of the main text, which we also duplicate here for convenience:

$$\frac{2\pi N}{\lambda_0} L + \phi = \pi(1 + m); m = 0, 2, 4, \dots \quad (\text{S5})$$

Neglecting dispersion of the reflection coefficient  $r(\lambda) = |r|e^{i\phi}$  (justified by Fig. 1(e) in the main text), we can differentiate Eq. (S5), with respect to wavelength, to find the change in resonance as a function of antenna length. First, we rewrite Eq. (S5) as

$$2\pi L(\lambda_0) = \frac{\lambda_0}{N(\lambda_0)} [\pi + \pi m - \phi] \quad (\text{S6})$$

and then differentiate to find

$$2\pi \frac{dL}{d\lambda_0} = \left( \frac{1}{N} - \frac{\lambda_0}{N^2} \frac{dN}{d\lambda_0} \right) [\pi + \pi m - \phi] \quad (\text{S7})$$

This expression can then be inverted to find the change in resonance wavelength as a function of antenna length (i.e., Equation (2) of the main text).

$$\begin{aligned} \frac{d\lambda_0}{dL} &= \frac{2\pi}{\pi + \pi m - \phi} \left( \frac{1}{N} - \frac{\lambda_0}{N^2} \frac{dN}{d\lambda_0} \right)^{-1} \\ &= \frac{2\pi}{\pi + \pi m - \phi} \frac{N^2}{N - \lambda_0 \frac{\partial N}{\partial \lambda}} \end{aligned} \quad (\text{S8})$$

## 2. ELLIPSOMETRY OF AL:ZNO AND ZNO FILMS

The optical properties of the Al:ZnO and ZnO films were obtained using spectroscopic ellipsometry (V-Vase, J.A. Woollam). The dielectric constants were obtained by fitting the retrieved data to the sum of a Drude and a Lorentz term. The values of our fit, along with the formula for our fit, are shown in Table S1. The permittivity of both our Al:ZnO film and the ZnO film is shown in Figures S1 and S2.

**Table S1. Ellipsometry Fit**

$$\varepsilon(\omega) = \varepsilon_\infty - \frac{\omega_p^2}{\omega(\omega + i\Gamma_p)} + \frac{f_l \omega_l^2}{\omega_l^2 - \omega^2 + i\omega\Gamma_l} \quad (\text{S9})$$

$\varepsilon_\infty$	$\omega_p$ (eV)	$\Gamma_p$ (eV)	$f_l$	$\omega_l$ (eV)	$\Gamma_l$ (eV)
2.5	2.32	0.089	15.02	4.53	0.001

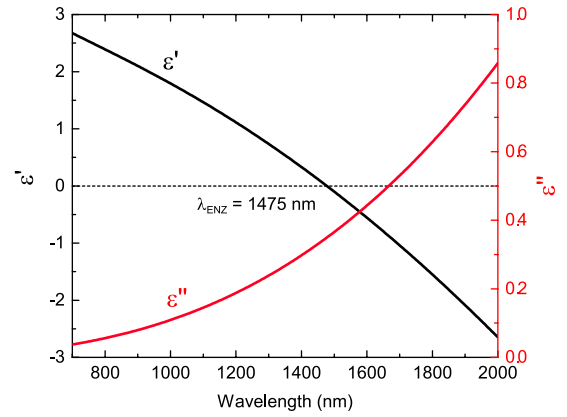


**Fig. S1.** Permittivity values of the Al:ZnO film extracted using spectroscopic ellipsometry. The ENZ wavelength is defined when real part  $\varepsilon' = 0$ .

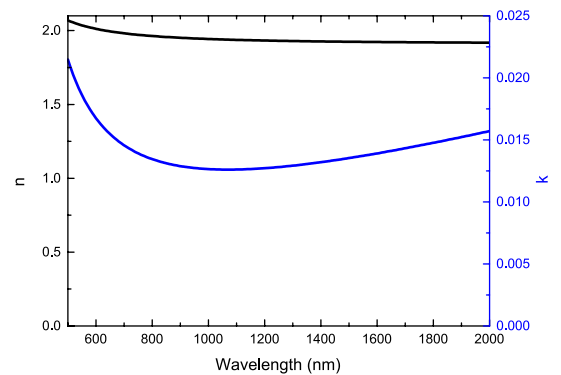


**Fig. S2.** Complex refractive index  $n + ik$  of ZnO film extracted using spectroscopic ellipsometry. Left axis (black line) is a real part of refractive index; right axis (blue line) is an imaginary part of refractive index, also known as extinction coefficient. ZnO's refractive index is approximately constant for all wavelengths of interest.

### 3. SAMPLE FABRICATION

We deposited Al:ZnO films via pulsed laser deposition (PVD Products, Inc.) onto glass substrates using a KrF excimer laser (Lambda Physik GmbH) operating at 248 nm. A 2wt% doped Al:ZnO target (>99.99% purity) from Kurt J. Lesker Corp. was used as the ablation source. The energy density of the laser at the target surface was maintained at  $1.5 \text{ J/cm}^2$  and the deposition temperature was fixed at  $95^\circ\text{C}$ . The optical properties of Al:ZnO films were characterized by spectroscopic ellipsometry (V-VASE, J.A. Woollam) over the spectral region from 400 to 2500 nm. To fabricate gold nanorods, positive electron beam resist (ZEP 520 A) was spin coated at 4000 rpm and then exposed by electron lithography (Vistec VB6). The beam energy was 100 kV and the beam current was 1.012 nA. We deposited a 40-nm-thick gold film on the resist using an electron beam evaporator. The sample was developed in ZED-N50 (n-amyl acetate) for 1 min, and then dipped in isopropyl alcohol for 30 s to remove the ZED-N50.

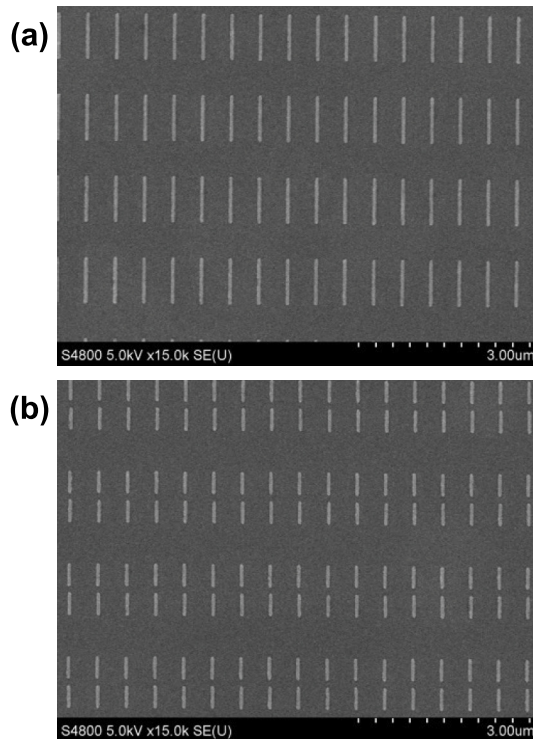


**Fig. S3.** Representative SEM image of (a) single and (b) dimer nanoantenna arrays deposited on Al:ZnO substrates.

### 4. FAR-FIELD MEASUREMENTS

We collected all far-field spectra using a VIS-NIR spectrometer (V-VASE, J.A. Woollam) equipped with focusing probes. The sample was mounted such that the long axis of the nanorods was oriented vertically. We set the input polarizer at  $45^\circ$  and the output analyzer at  $-45^\circ$  and collected the reflected light over a 900–2500 nm spectrum. The angle of incidence was set at  $18^\circ$  — the minimum physical angle of the ellipsometer. Collected spectra were then fitted using a standard Lorentzian function, which was then used to calculate the central resonance wavelength.

### 5. NEAR-FIELD MEASUREMENTS

Near-field maps were obtained using a commercial scattering-type SNOM (Neaspec GmbH). For the experiments, we used Platinum-coated standard Si atomic force microscope tips (Arrow™ NCPt from NanoWorld) operated in a tapping-mode. The tip radius of curvature of less than 25 nm is specified by the manufacturer. The tapping frequency and amplitude were  $\sim 280 \text{ kHz}$  and  $\sim 50 \text{ nm}$ , correspondingly. We illuminated all samples normally from beneath using a tunable telecom diode laser (TLB-6500-H-ES from New Focus) and a parabolic mirror. The spot size on the sample was approximately  $\sim 50 \mu\text{m}$  and the incident total power was maintained at  $\sim 1 \text{ mW}$ . Scattered light was collected using a second parabolic mirror. A Mach-Zehnder interferometer with an oscillating mirror ( $f \sim 300 \text{ Hz}$ ) in the reference arm is incorporated in our SNOM in order to resolve both amplitude and phase using a pseudo-heterodyne detection scheme [1]. To remove background signals, the collected output was demodulated at the third harmonic of the tip's tapping frequency.

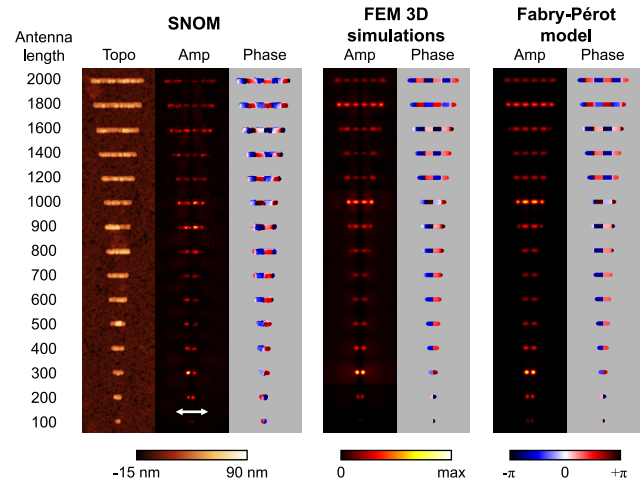


**Fig. S4.** Comparison of experimental and simulated near-field maps of gold antennas on ZnO substrate at 1500 nm excitation, polarized along the antenna length. Left column contains the measured topography, the magnitude, and the phase of the near-field. The polarization of incident wave is shown with a white arrow. Middle and right columns are the corresponding  $z$ -component of the electric field ( $E_z$ ) calculated at 50 nm above nanorods with full 3D finite-element simulations and semi-analytical Fabry-Pérot model, respectively. Geometric cross-sections of the antennas were used for masks in phase maps.

### 6. NUMERICAL SIMULATIONS

Simulations were done in COMSOL software using 2D [for mode analysis, Figs. 1(b-d)] and 3D FEM calculations. Permittivity values of gold were taken from Palik handbook [2], while values of Al:ZnO and ZnO were extracted from spectroscopic ellipsometry. The glass substrate was assumed to have a constant refractive index of 1.45. All edges of gold bricks were rounded with 10 nm radius of curvature. Simulation domains were squares (2D FEM) or cubes (3D FEM) with edge size of  $4 \mu\text{m}$ , surrounded with perfectly matching layers.

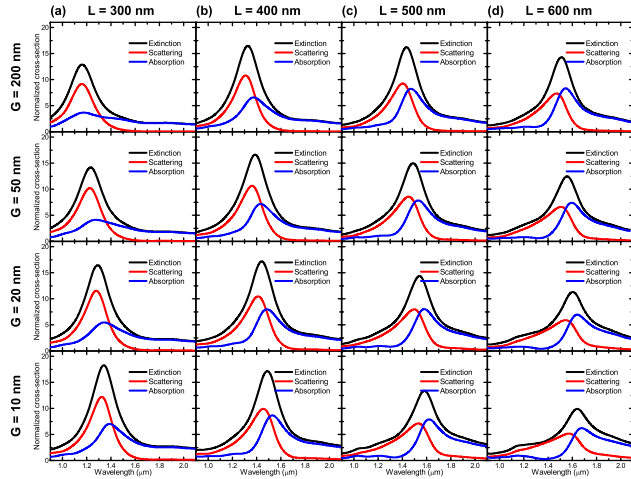


**Fig. S5.** Normalized extinction, scattering, and absorption cross-sections (black, red, and blue lines, respectively) for single antennas on Al:ZnO of a) 300, b) 400, c) 500, and d) 600 nm single antenna lengths and gap distance of  $G = 200$ , 50, 20 and 10 nm. For decreasing gap sizes, the red-shift in absorption and scattering cross-sections is because of the dipole-dipole interaction between individual nanorods. For individual nanorods which resonate at a wavelength at or longer than the ENZ wavelength of the Al:ZnO substrate (1475 nm), the red-shift is reduced and the amplitude is diminished. Additionally, the absorption cross-sections increase, corresponding to the increase in the imaginary portion of the effective index.

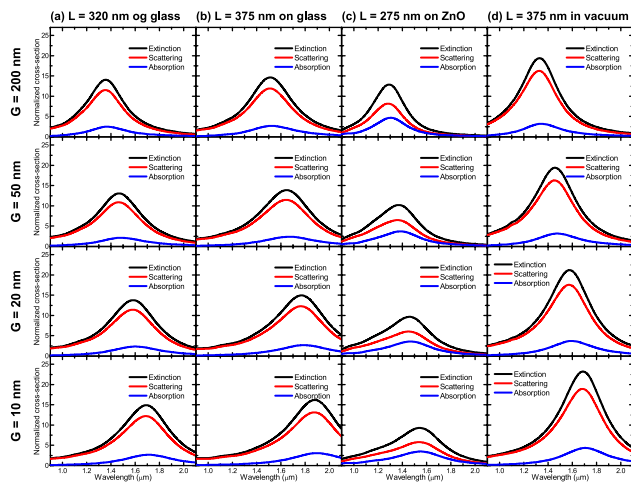


**Fig. S6.** Normalized extinction, scattering, and absorption cross-sections (black, red, and blue lines, respectively) for dimer antennas on glass ( $n = 1.45$ ), ZnO, and vacuum. For comparison, the individual antenna lengths are chosen such that the shift in resonance crosses the ENZ point of the Al:ZnO substrate (1475 nm).

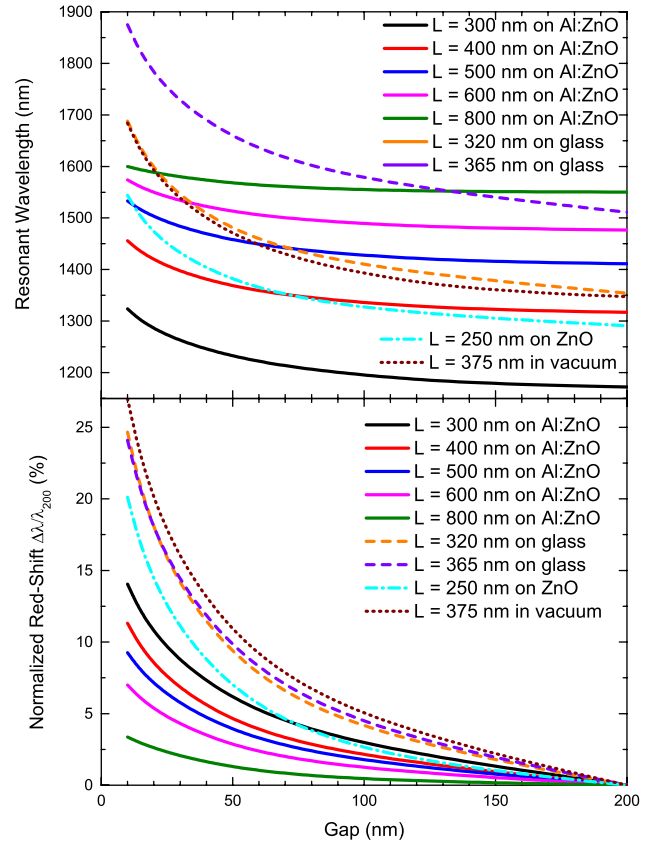


**Fig. S7.** Resonance wavelength of dimer antennas as a function of gap size and antenna length. The resonance wavelength was calculated as a position of the peak in the simulated extinction spectra (Figures S5-S6). Bottom image shows a shift of the resonance wavelength for dimer antennas, normalized to the resonance wavelength of dimer antennas with a 200-nm gap. The shift is reduced with a decrease of antenna length for ENZ substrate, while it is nearly the same for antennas on a glass and ZnO substrate or in vacuum.

## REFERENCES

1. N. Ocelic, A. Huber, and R. Hillenbrand, "Pseudo-heterodyne detection for background-free near-field spectroscopy," *Appl. Phys. Lett.* **89**, 101124 (2006).
2. E. D. Palik, ed., *Handbook of Optical Constants of Solids. Handbook of Optical Constants of Solids* (Academic Press, New York, 1985).